Design and Analysis of Slotless Brushless DC Motor

Jung-Moo Seo, Joo-Han Kim, In-Soung Jung, *Senior Member, IEEE*, and Hyun-Kyo Jung, *Senior Member, IEEE*

Abstract—**This paper presents a design method for a small-sized slotless brushless dc motor. Distributed hexagonal windings are employed for achieving a high torque density and for ease of manufacture. Numerical approaches with an analytic model are used to analyze the magnetic and output characteristics of the motor. The proposed motor is manufactured, and the empirical results are compared with the results of the simulation.**

Index Terms—**Brushless dc (BLDC) motor, hexagonal winding, slotless motor.**

I. INTRODUCTION

THE brushless dc (BLDC) motor has been used in various applications due to its high efficiency, power density, and excellent controllability. However, the stator core in the conventional structure prevents the overall size of the motor from minimizing; moreover, the winding process becomes progressively more difficult as the motor shrinks in size. The slotless BLDC motor, which has either concentrated or distributed windings fixed on the cylindrical stator iron, has several advantages as well as minimizing merit. The size of the permanent magnet of the rotor can be increased due to the slotless stator structure, the torque density is bigger than that of the slotted motor [1], the cogging torque is extremely small, and the vibrations and noise can be reduced. The winding that is placed in the air gap is profitable for cooling because the heat generated from the winding can be removed not only through the iron but also by the air that moves in the gap [2].

Most previous studies have dealt with slotless BLDC motors from an analytic point of view to design and analyze the output characteristics; furthermore, a rectangular winding is considered. Reference [3] describes a 2-D analytical model for predicting the winding inductance and armature reaction field of slotless BLDC motors. In [2], parametric analysis is conducted for the winding and permanent-magnet dimensions but is limited in preliminary design; furthermore, there is no comparison between the predicted and actual results in manufacturing. In [1], [4], and [5], analytic approaches are presented to calculate the air gap flux density and induced torque; furthermore, a general rectangular coil winding is considered

Fig. 1. Diagram of a slotless BLDC motor with a two-pole double-layered winding. Nine single coils are distributed in the stator core.

and manufactured. However, the specific winding shape and arrangement are not considered.

Based on finite-element (FE) analysis, this paper presents the design of a small-sized slotless BLDC motor. Through numerical analysis, the basic dimensions are ascertained, and the winding features are determined. Then, the induced voltage is calculated, and the variation of the rotational speed and current with respect to the torque is estimated through analytic equations. The designed motor is manufactured, and the output characteristics are compared with those of the simulated one.

II. BASIC STRUCTURE

Fig. 1 shows a diagram of an inner rotor slotless BLDC motor. We designed a two-pole three-phase motor with a double-layered short-pitch winding. A ring-shaped high-energy permanent magnet (sintered NdFeB) is used, and a distributed winding composed of nine single coils is fixed on the stator core. In order to determine the geometric parameters of the motor for a given constraint on the outer size, the flux density distribution is calculated. For achieving a high torque density, the size of the permanent magnet is maximized as much as possible, and the flux density of the stator core is estimated with respect to various magnet volumes. Through back electromotive force (EMF) calculation, the winding area is roughly determined on the basis of the number of coil turns.

There are several types of winding for slotless BLDC motors. A rectangular winding is profitable for increasing the linkage flux and forming the winding arrangement; however, the end-turn parts that are generated at both the top and bottom sides can be an obstacle to combine with the windings and stator core. Furthermore, the thickness of the end turn is proportional to the coil pitch, which necessitates additional work for enlarging the space for rotor positioning. In a rhombic winding structure, we do not need to consider the end-turn parts, but the back EMF at the same rotational speed and magnetic condition is much less than that for a rectangular structure. Fig. 2 shows a
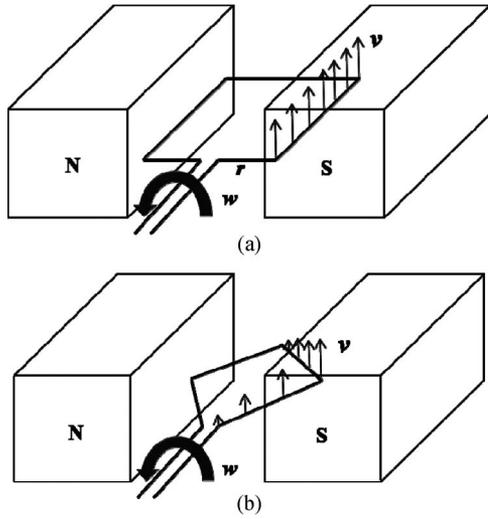
Fig. 2. Concept diagram of rectangular and rhombic windings. (a) Rectangular loop. (b) Rhombic loop. In the rhombic loop, the velocity of the conductor is dependent on the axial position.

concept diagram that presents the induced EMF values of the rectangular and rhombic windings. The EMF that is induced from the conductor that moves in the magnetic field can be expressed as

$$E_{\mathrm{ind}} = (v \times B) \cdot l \tag{1}$$

where v is the velocity of the conductor, B is the magnetic flux density, and l is the length of the conductor. v can be replaced as follows:

$$v = r\omega \tag{2}$$

where r is the radius of the loop and ω is the angular velocity. In the rectangular loop, the radius of the loop is constant in the overall axial points; however, in the rhombic loop, the radius varies with respect to the axial length. This means that, when the loop rotates, the velocity of the conductor is different at every point in the rhombic loop. Therefore, the induced EMF is different and smaller than that in the case of the rectangular loop. From this point of view, a hexagonal winding, which is partly composed of rectangular and rhombic structures, has advantages in terms of both magnetic and manufacturing aspects. Since the coil side is perpendicular to the flux from the permanent magnet, the linkage flux of the coil is increased, and the ends of the winding are not thick owing to the oblique coil sides of both end sections as in rhombic windings.

III. NUMERICAL DESIGN

To simulate the hexagonal winding in 2-D, we segment the winding into several slices along the axial direction, as shown in Fig. 3. The EMF that is induced from the perpendicular side of the coil (region ④) can be calculated in conventional 2-D analysis, but in order to figure out the EMF from the oblique side (regions ①, ②, and ③), coil reassignment with respect to the sliced region is required. As can be seen in this figure, the coil pitch increases with the index of the region. The back EMF regarding each sliced region is calculated, and the summation
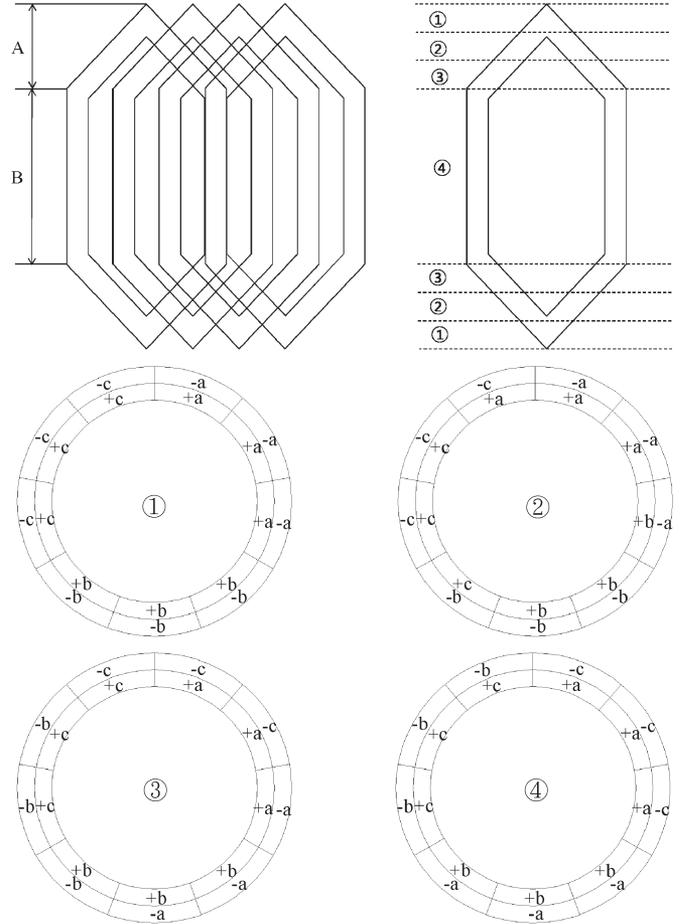
Fig. 3. Sliced regions for 2-D analysis and the winding arrangement with respect to the regions.

of the values, considering the axial length, is finally determined. That is, if the EMF values per unit length of the four regions are E_1, E_2, E_3, and E_4, respectively, and the lengths of the coil along the oblique and perpendicular sides are A and B, respectively, the total induced back EMF E_t is shown in Fig. 4 and expressed as

$$E_t = 2(E_1 + E_2 + E_3)A/(\text{the number of regions}) + E_4 B. \tag{3}$$

Due to the characteristics of the numerical methodology as previously mentioned, the number of sliced regions can affect the accuracy of the simulation results. Fig. 5 shows the results of the back-EMF calculation with respect to the number of sliced regions. As the number increases, the EMF increases before converging to a constant value.

A 3-D FE analysis is performed, and the results are examined to verify the result from the proposed 2-D analytical method. We model a hexagonal winding in 3-D and calculate the back EMF. Fig. 6 shows the 3-D FE model and the results from both the 3-D analysis and the proposed method; the two sets of results are in reasonable agreement. We confirm that, if a proper correction factor is used in the computational process, we can accomplish the analysis much more quickly.

From the back-EMF calculation, the EMF constant is induced and applied in the voltage equation for the dc motor to
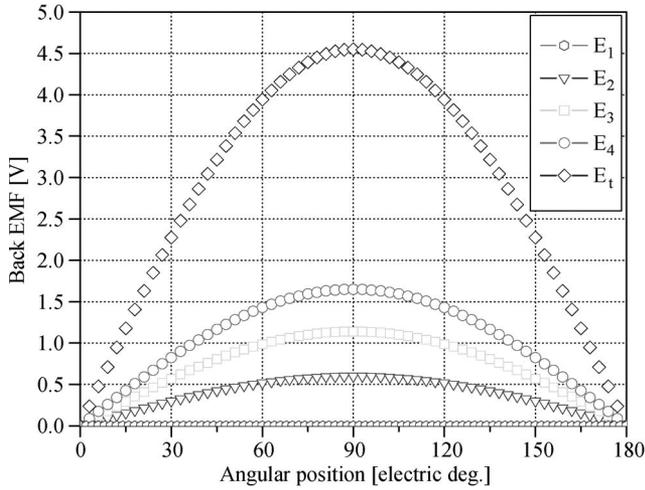
Fig. 4. Back-EMF calculation for various sliced regions per phase. The rotational speed is 10 000 r/min.
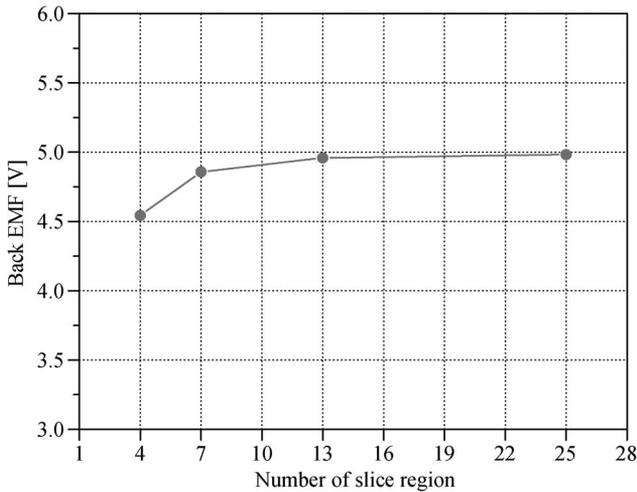
Fig. 5. Back-EMF calculation with respect to the number of sliced regions.

Fig. 6. Three-dimensional FE model and the back-EMF results. Using the proposed method, much faster analysis can be accomplished. (a) 3-D FE model. (b) Comparison of the back-EMF values from the proposed 2-D method and 3-D FE analysis.
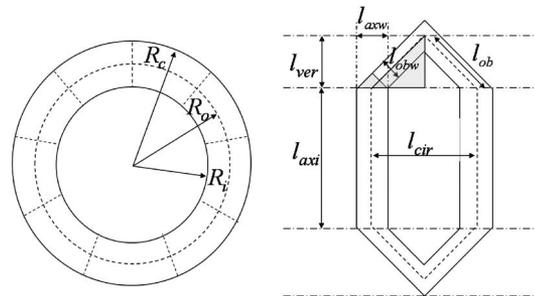
Fig. 7. Cross section of the winding part and specification of a single coil.

predict the output characteristics, such as the speed and torque. The rotational speed from the voltage equation is given by

$$\omega = \frac{V_t}{K_e} - \frac{R_a T}{K_e^2} \qquad (4)$$

where V_t is the applied voltage, K_e is the EMF constant, R_a is the winding resistance, and T is the developed torque. V_t is fixed, and K_e is calculated as previously mentioned. If we ascertain the value of R_a, the speed and current characteristics with respect to the torque variation are determined.

The circumferential length between both the coil sides in Fig. 7 is

$$l_{\text{cir}} = \frac{3}{9} \times 2\pi R_o \qquad (5)$$

where R_o is the radius of the median circle with respect to the double-layered winding. The oblique line length is

$$l_{\text{ob}} = \sqrt{\left(\frac{l_{\text{cir}}}{2}\right)^2 + l_{\text{ver}}^2}. \qquad (6)$$

The conductor length that is used to wind a phase is

$$l_{\text{ph}} = N_p(2l_{\text{axi}} + 4l_{\text{ob}}) \qquad (7)$$

where l_{ver} is the vertical length of the oblique line, l_{axi} is the axial length, and N_p is the number of turns per phase. Therefore, the phase resistance is given by

$$R_{\text{ph}} = \rho \frac{l_{\text{ph}}}{S_c} \qquad (8)$$

where ρ is the copper specific resistance and S_c is the cross-sectional area of the conductor.

TABLE I
FINAL MOTOR DESIGN

Item	Value
Motor type	2 pole / 9 coils
Driving voltage [V]	12
Rated output power [W]	15
External diameter of stator yoke [mm]	21.0
Internal diameter of stator yoke [mm]	15.0
External diameter of magnet [mm]	10.4
Internal diameter of magnet [mm]	3.2
Axial length of stator core and magnet [mm]	26
Air gap [mm]	0.3
Permanent magnet remanence [T]	1.26 (sintered NdFeB)
Number of turns/phase	33
Coil diameter [mm]	0.26 (two-wired)

Fig. 9. Winding manufacturing process.

Fig. 8. Estimation of the N–T–I characteristics of the proposed motor.

A slotless motor can possess a higher winding fill factor compared to a slotted type due to the construction of the toothless stator core. In the hexagonal distributed winding, the usable area for the conductor is governed by the oblique linewidth of the winding; furthermore, accurate estimation of the winding fill factor is required for organizing an effective magnetic circuit. The oblique linewidth of the winding is given by

$$l_{\text{obw}} = \frac{l_{\text{axw}} l_{\text{ver}}}{l_{\text{ob}}} \text{ (from the similarity of triangles)} \quad (9)$$

where l_{axw} is $l_{\text{cir}}/3$ (the coil pitch is three in this paper). The surface area of one winding side is

$$S_w = l_{\text{obw}}(R_c - R_o) \quad (10)$$

where R_c is the external diameter of the stator yoke.

Therefore, the winding fill factor is

$$W_f = \frac{N_p}{3} \frac{S_c}{S_w}. \quad (11)$$

The final specifications are given in Table I. With the parameters determined as previously mentioned, the speed, torque, and input current are calculated in Fig. 8.

(a)

(b)

(c)

Fig. 10. Assembled slotless BLDC motor. (a) Exploded diagram. (b) Rotor and stator element. (c) Assembled motor.

IV. MANUFACTURING AND VERIFICATION

Fig. 9 shows the procedure for manufacturing the winding. Self-bonding magnetic wires are prepared, and single coils are
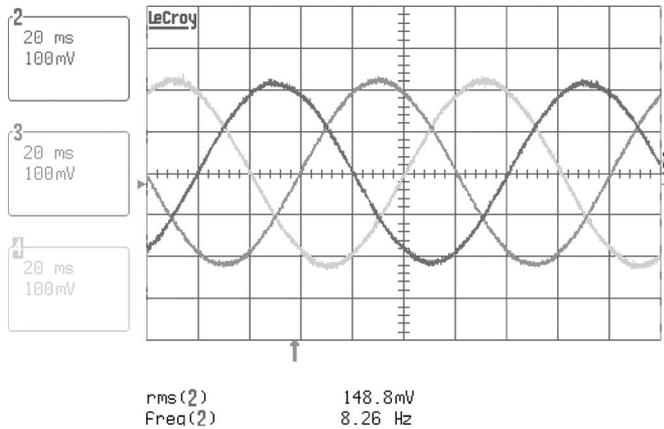
Fig. 11.　Measured back EMF induced in each phase coil. The rotational speed is 500 r/min (20 ms/division and 100 mV/division).
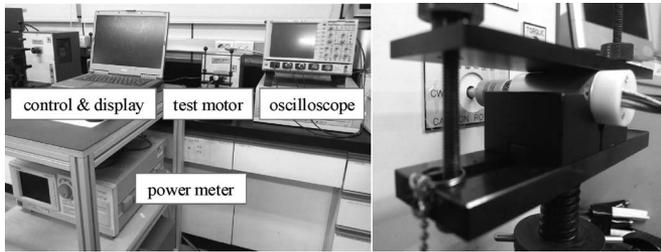
Fig. 12.　Assembled slotless BLDC motor.

produced using a hexagonal winding fixture. Those coils are arranged on the external surface of a winding assembly jig considering the radial lengths of the permanent magnet and the air gap. For an accurate arrangement of the single coils, special grooves are formed between the perpendicular sides of adjacent coils on the assembly jig. Tiny pins are put into the grooves, and the single coils are arranged with a constant gap owing to the pins. Following the winding lineup, we remove the pins from the assembly jig and push the outer part of the winding using a pressing jig. This causes the winding to form well and to conform to the intended dimensions. The winding is inserted in the stator core with insulating material, and heat is applied to the stator core to fix and again bond the contiguous wires.

Fig. 10 shows an exploded diagram of the assembled motor. The stator core is bonded to the housing, and the rotor, along with the shaft and permanent magnet, is set inside. A Hall IC and a sensing magnet are installed in the rear housing of the motor for positional detection and proper timing of switching.

The three-phase back EMF of the manufactured motor at 500 r/min is shown in Fig. 11. Even though the winding assembly is built in-house, the values and shapes of the EMFs are very similar. The measured EMF is 220 mV_{0-peak}, which shows a good agreement compared with the predicted value in Figs. 4 and 6. Both the distributed winding and the parallel magnetization of the permanent magnet cause the waveform of the EMF to be sinusoidal. A square-wave current waveform is applied in this paper; however, with sine-wave current control, soft driving with a little torque ripple is possible.

For the loading torque test, the manufactured motor is connected to the torque measuring system, as shown in Fig. 12.
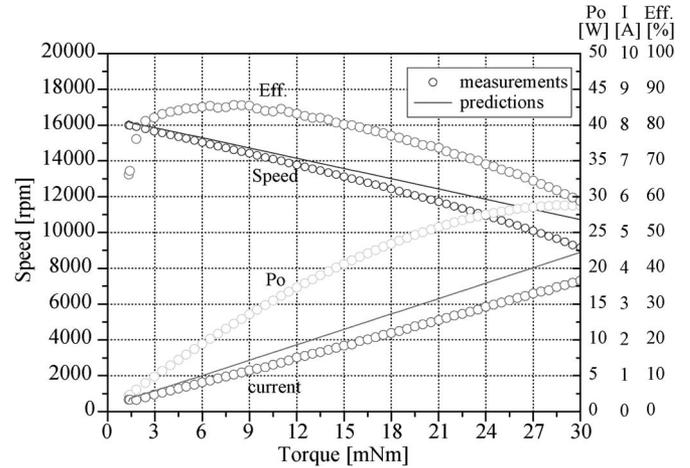
Fig. 13.　Experimental results for the designed motor.

The measurement equipment consists of a dc power supply, a dynamometer for estimating the output characteristics, a power meter for calculating the input power, and a laptop computer for display and load control.

Fig. 13 shows the output characteristics of the manufactured motors. As can be seen in this figure, no load speed is more than 16 000 r/min, and the efficiency is about 80% at an output power of 20 W, while the maximum efficiency is 85%. By comparing with the simulated results in Fig. 8, a reasonable agreement is seen to be achieved. As the loading torque increases, the rotational speed and input current decrease compared to the experimental results, which could be due to the resistance increase and voltage drop. If the core loss calculation with regard to various loads is conducted in future work, more accurate estimation can be possible.

V. CONCLUSION

In this paper, a slotless BLDC motor has been designed and analyzed. The stator core is composed of double-layered short-pitch windings with nine hexagonal single coils, and a two-pole permanent magnet is applied in the rotor. To simulate the hexagonal windings in 2-D, the winding is divided into several sliced regions along the axial direction. The EMF constant is determined by summing up each region's EMF value, and the voltage equation is used to predict the output characteristics. The proposed motor was manufactured; finally, the experimental results were compared with the simulated results.

REFERENCES

[1] N. Bianchi, S. Bolognani, and F. Luise, "Analysis and design of PM brushless motor for high-speed operations," *IEEE Trans. Energy Convers.*, vol. 20, no. 3, pp. 629–637, Sep. 2005.
[2] Y. Chen, J. Shen, and Z. Fang, "Topology and preliminary design of slotless brushless dc motor," in *Proc. IEMDC*, 1997, pp. WB2/7.1–WB2/7.3.
[3] K. Atallah and Z. Q. Zhu, "Armature reaction field and winding inductances of slotless permanent-magnet brushless machines," *IEEE Trans. Magn.*, vol. 34, no. 5, pp. 3737–3744, Sep. 1998.
[4] N. Bianchi, S. Bolognani, and F. Luise, "High speed drive using a slotless PM motor," *IEEE Trans. Power Electron.*, vol. 21, no. 4, pp. 1083–1090, Jul. 2006.
[5] M. Markovic and Y. Perriard, "Simplified design methodology for a slotless brushless dc motor," *IEEE Trans. Magn.*, vol. 42, no. 12, pp. 3842–3846, Dec. 2006.

Jung-Moo Seo was born in Kyunggi, Korea, in 1976. He received the B.S. degree from the School of Electrical and Electronics Engineering, Chung-Ang University, Seoul, Korea, in 2003, and the M.S. degree from the School of Electrical Engineering, Seoul National University, Seoul, in 2005.

He is currently with the Intelligent Mechatronics Research Center, Korea Electronics Technology Institute, Bucheon, Korea, where he works on the development of electric machinery and actuators.

In-Soung Jung (S'93–M'00–SM'07) received the B.S. degree in electronics engineering and the M.S. and Ph.D. degrees in electrical engineering from Hanyang University, Seoul, Korea, in 1993, 1995 and 2000, respectively.

Since 2000, he has been the Director of the Intelligent Mechatronics Research Center at the Korea Electronics Technology Institute, Bucheon, Korea, where he works on the development of electric machines and systems.
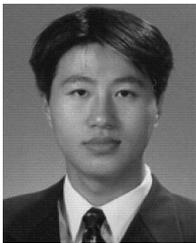
Joo-Han Kim received the B.Sc. degree from Sogang University, Seoul, Korea, and the M.Sc. degree from Yonsei University, Seoul.

He is currently with the Korea Electronics Technology Institute, Bucheon, Korea, where he was a Senior Researcher and has been a Meca Team Manager of the Intelligent Mechatronics Research Center since 1999. His research interests include actuator mechanism design and fan/blower design and analysis.

Hyun-Kyo Jung (S'82–M'90–SM'99) graduated in 1979 from the School of Electrical Engineering, Seoul National University, Seoul, Korea, where he also received the M.S. and Ph.D. degrees in 1981 and 1984, respectively.

He was a faculty member at Kangwon National University, Korea, from 1985 to 1994. From 1987 to 1989, he was with the Polytechnic Institute of New York University. Since 1994, he has been a Professor at Seoul National University. From 1999 to 2000, he was a Visiting Professor at the University of California, Berkeley. His research interests cover the various fields of the analysis and design of electric machinery and numerical field analysis of electrical systems, in particular, with the finite-element method.